Orientation and motion of a plasma discontinuity from single-spacecraft measurements: Generic residue analysis of Cluster data

B. U. Ö. Sonnerup,[1] S. Haaland,[2,3] G. Paschmann,[2,4] M. W. Dunlop,[5] H. Rème,[6] and A. Balogh[7,8]

Received 18 November 2005; revised 17 January 2006; accepted 26 January 2006; published 12 May 2006.

[1] A unified minimum-residue approach is presented to the use of classical conservation laws for determination of the orientation and motion of a plasma discontinuity, using data from a single spacecraft that traverses the discontinuity and makes measurements, not only on its two sides but also within it. The method is a generalization of the minimum Faraday residue (MFR) analysis technique described by Khrabrov and Sonnerup (1998a). It includes not only the standard MHD conservation laws for mass, momentum, total energy, and (where applicable) entropy, but also magnetic flux conservation from Faraday's law, absence of magnetic poles from $\nabla \cdot \mathbf{B} = 0$, and electric charge conservation from Ampère's law. A method, denoted by COM, for combining the results from more than one conservation law into a single optimal determination of the orientation and motion is presented, along with a general approach to the application of a certain class of constraints that can be placed on the vector normal to the discontinuity. The methodology, which is applicable to many types of discontinuity, including shocks, is illustrated by analysis of one magnetopause encounter by two of the four Cluster spacecraft (C1 and C3). The results from the various individual methods have considerable spread. However, in favorable circumstances and by exercising considerable care, the vector normal to the magnetopause from COM can be accurate to within a couple of degrees. For the C1 crossing, believed to be nearly a tangential discontinuity, albeit with signatures of incipient reconnection, the magnetopause speed (-56 km s^{-1}) from COM appears accurate to within a few km s^{-1}. The plasma flow across the magnetopause and the normal field component are both very nearly zero, and the results are consistent with those obtained from timing of the layer as it crosses the four Cluster spacecraft (assuming a constant thickness of the layer). The results for the velocity of the magnetopause and for the plasma flow across the layer are less consistent for the C3 crossing, believed to be a rotational discontinuity. For this crossing the presence of a component of the magnetic field along the normal direction could not be established with certitude. It is likely that the lower quality of the results for this crossing is caused by local multidimensional structure of the magnetopause.

Citation: Sonnerup, B. U. Ö., S. Haaland, G. Paschmann, M. W. Dunlop, H. Rème, and A. Balogh (2006), Orientation and motion of a plasma discontinuity from single-spacecraft measurements: Generic residue analysis of Cluster data, *J. Geophys. Res.*, *111*, A05203, doi:10.1029/2005JA011538.

[1]Thayer School of Engineering, Dartmouth College, Dartmouth, New Hampshire, USA.
[2]Max-Planck-Institut für Extraterrestrische Physik, Garching, Germany.
[3]Also at Department of Physics and Technology, University of Bergen, Bergen, Norway.
[4]Formerly at International Space Science Institute, Bern, Switzerland.
[5]Space Sciences Division, Rutherford Appleton Laboratory, Chilton, UK.
[6]Centre d'Étude Spatiale des Rayonnements, Toulouse, France.
[7]Space and Atmospheric Physics Group, Imperial College, London, UK.
[8]Also at International Space Science Institute, Bern, Switzerland.

0148-0227/06/2005JA011538$09.00

1. Introduction

[2] To study the shape and motion of the magnetopause surface, moderately accurate determinations of **n**, the vector normal to the layer, and u_n, the speed of the magnetopause along that normal, are sufficient. Information about **n** and u_n allows detailed, quantitative study of wave motion and of other deformations of the magnetopause surface. It also allows determination of the magnetopause thickness and its variations, as well as the current density magnitudes and distribution within it, results that are important for the study of plasma instabilities and other processes that may be operating in the layer. These statements also apply to shocks and other discontinuities observed in space plasmas. However, the magnetopause application poses the most stringent requirements on the accuracy of the results and therefore provides a suitable testing ground for new techniques. Direct measurements of magnetic connection and convective or diffusive plasma flow across the magnetopause are important objectives that require extremely accurate determination of the orientation and speed of the current layer. The reason is that, at the magnetopause but not at the bow shock, the magnetic field and plasma flow components across the layer are usually very small (<10%) compared to the total field and flow magnitudes. Thus, even a small error in the normal vector will produce large uncertainties in the normal field and flow component. Additionally, the latter is very sensitive to errors in the magnetopause speed. Perhaps the most important transport process operating in the magnetopause is magnetic reconnection. It causes the development of a normal magnetic field component and an associated normal flow component, which are proportional to each other and are related to the reconnection rate. This rate is usually small and has proved difficult to determine in a reliable way from in situ measurements of magnetic field and plasma flow. Yet, the reconnection rate remains an important aspect of many magnetopause studies and the goal of determining it with sufficient accuracy is one motivation for the efforts reported here, to broaden and improve the set of data analysis techniques.

[3] The first attempts to address the question of magnetopause orientation and normal magnetic field component were based on minimum-variance analysis of magnetic field vectors measured by a single spacecraft during a magnetopause traversal (MVAB) [*Sonnerup and Cahill*, 1967]. The magnetopause speed at that time was inferred, not from in situ plasma velocity measurements, since such measurements were either unavailable or had too low accuracy, but from various indirect methods. The results of the latter did not permit determination of the plasma flow speed across the magnetopause. A few results from MVAB have been reported where a significant normal magnetic field component was present [e.g., *Sonnerup and Ledley*, 1979], but the most common result is either that the normal component is too small to exceed expected uncertainties, or that the normal direction is grossly incorrect as a result of multidimensional substructures or near degeneracy of the variance matrix. With the advent of the ISEE and AMPTE missions, plasma instruments, and also electric field measurements, had developed to the point where the deHoffmann-Teller (HT) frame velocity, $\mathbf{V}_{HT}$, could be reasonably well determined. The HT frame velocity is obtained from a least squares procedure, on the basis of the requirement that the electric field or, in the case of plasma measurements, the convection electric field, $-\mathbf{v}\times\mathbf{B}$, should be a minimum in the HT frame [*Sonnerup et al.*, 1987; *Khrabrov and Sonnerup*, 1998b]. (In the first practical application of the HT frame at the magnetopause, electric and magnetic fields measured by ISEE were used and the frame velocity was determined by trial and error [*Aggson et al.*, 1983]). Once $\mathbf{V}_{HT}$ is known, the magnetopause speed is given by $u_n = \mathbf{V}_{HT}\cdot\mathbf{n}$ and the plasma flow speed across the magnetopause is $v'_n = \langle\mathbf{v}'\rangle\cdot\mathbf{n} = (\langle\mathbf{v}\rangle\cdot\mathbf{n} - u_n)$, where $\mathbf{v}' = \mathbf{v} - \mathbf{V}_{HT}$ is the plasma velocity in the HT frame. Here, and in what follows, the angle brackets denote the average over a set of quantities measured during the crossing. With an outward directed normal, one expects v'_n to be negative because the flow across the magnetopause should be from the magnetosheath into the magnetosphere, except in unusual circumstances. It has turned out that in practice the HT frame velocity and the normal (and probably the measured plasma velocities as well) were not sufficiently accurately determined to yield reliable values of v'_n. The magnitude of this velocity component is expected to be rather small, typically in the range 0–20 km s^{-1}.

[4] A trial-and-error method for determination of both **n** and u_n in a single calculation was developed by *Terasawa et al.* [1996] and was subsequently cast in a convenient least-squares form by *Khrabrov and Sonnerup* [1998a]. This method is referred to as Minimum-Faraday-Residue (MFR) analysis. It is based on the fact that in a frame moving with a one-dimensional current layer of time-invariant structure, Faraday's law requires the two components of the electric field tangential to the layer to be constant throughout the layer. The method can be used either with directly measured electric fields or, more commonly, with the convection field, $-\mathbf{v}\times\mathbf{B}$, serving as a proxy for the electric field. Additionally, measured magnetic fields are needed and, as a consequence of the divergence of Faraday's law, MFR incorporates the condition $\nabla\cdot\mathbf{B} = 0$; that is, it incorporates the condition upon which the MVAB determination of **n** and $B_n = \langle\mathbf{B}\rangle\cdot\mathbf{n}$ is based. Experience has shown that this method can give reasonable results, even for some events where the MVAB/HT technique is near degeneracy and fails to give believable values of **n**, B_n and u_n. However, the accuracy is still usually insufficient for reliable determination of v'_n, the plasma flow speed across the moving magnetopause. This is also the case for a recently developed technique that is based on mass conservation and is referred to as the Minimum Mass-flux Residue (MMR) method [*Sonnerup et al.*, 2004]. In this analysis, only measured plasma velocities and densities, but not the magnetic fields, are needed. Use of MFR and MMR with Cluster data have indicated good consistency between the two methods, although v'_n, the plasma flow speed across the magnetopause, has remained elusive. The reasons for the uncertainty in the results for this flow speed may lie as much in violations of the model assumptions upon which the various methods are based, as in inaccuracies of the actual measurements.

[5] The development of MMR makes clear that a minimum residue approach can be applied, not only to mass conservation, but to any standard conservation law, such as momentum and energy conservation. The use of these laws

Table 1. Acronyms

Method	Acronym[a]
deHoffmann-Teller frame determination	HT
Grad-Shafranov reconstruction	GS
Constant velocity approach	CVA
Constant thickness approach	CTA
Minimum thickness variation	MTV
Discontinuity analyzer	DA
Minimum variance analysis of **B** field	MVAB
Minimum variance analysis of current	MVAJ
Minimum variance analysis of $\nabla \times \mathbf{E}$	MVACE
Minimum variance analysis of $\partial\mathbf{B}/\partial t$	MVADB
Minimum variance analysis of **v**	MVAV
Minimum Faraday residue analysis	MFR
Minimum mass flux residue analysis	MMR
Minimum linear momentum residue analysis	MLMR
Minimum total energy residue analysis	MTER
Minimum entropy residue analysis	MER
Composite approach	COM

[a]To these acronyms the symbols $\perp_1 - \perp_6$ from Table 2 may be added to indicate various types of constraints.

in discontinuity analysis is not new. They were applied a long time ago, and in various forms, to shocks [e.g., *Lepping and Argentiero*, 1971; *Vinas and Scudder*, 1986]. In these applications, use was made only of the shock jump conditions (the Rankine-Hugoniot relations) and data taken on the two sides of the shock but not of the full momentum equation and data taken within the shock layer itself. More recently, *Kawano and Higuchi* [1996] included the conservation laws in a generalized minimum variance approach, based on multiplication of variances, which has however not found widespread use. The approach we present in this paper is additive. It has the advantage of being simple to implement in a generic form, which can then be adapted to each individual conservation law and which also provides a convenient way to combine the conservation laws to obtain a single prediction for the normal vector, the magnetopause speed, and the components of magnetic field and plasma flow across the layer. The result is optimal in the sense that all relevant, measured information enters into the calculation. We also show how various constraints on the normal vector's orientation can be conveniently implemented. The combination (COM or COM*) of results from different conservation laws and the technique for implementing constraints were used by *Sonnerup et al.* [2004]. In the present paper these items will be more fully explained.

[6] Our paper is concerned exclusively with single-spacecraft methods. Multispacecraft methods have been reviewed recently by *Haaland et al.* [2006] and *Dunlop et al.* [2006]. Our paper is organized as follows. In section 2, we present the generic form of the minimum residue analysis, as applied to a classical conservation law. Section 3 contains the applicable formulas for each specific conservation law. In section 4, we show how a certain class of constraints on the normal-vector orientation can be implemented, and in section 5 how the applicable conservation laws can be combined to provide a single optimal result. Application to two Cluster encounters with the magnetopause are given and discussed in section 6. For convenient reference, the acronyms used for the different methods are listed in Table 1. For historical reasons, all methods that are based on the vanishing of the divergence of a vector quantity are referred to as Minimum Variance Analysis whereas all methods that are based on a full conservation law, including both the time derivative and the divergence term, are called Minimum Residue Analysis.

2. Generic Minimum Residue Analysis

[7] In order to accommodate the conservation of vector quantities, such as momentum, as well as scalar quantities, such as mass, in our generic development, we adopt Cartesian index notation and the Einstein summation convention (repeated indices are summed over). Thus we write the generic conservation law as

$$\frac{\partial}{\partial t}\eta_i + \frac{\partial}{\partial x_j} q_{ij} = 0, \tag{1}$$

where η_i is the density of the conserved quantity and q_{ij} is the corresponding transport tensor. For example, in the case of linear momentum conservation, $\eta_i = \rho v_i$, is the momentum density component along the axis x_i (i = 1, 2, 3) and q_{ij} is the complete momentum transport tensor, the convective part of which is $\rho v_i v_j$. Also, in (1), the repeated index, j, (j = 1, 2, 3) is summed over. Thus the second term in (1) is the divergence of q_{ij}. The conservation of mass illustrates the conservation of a scalar quantity: Here $\eta_i = \rho$ is the mass density and $q_{ij} = \rho v_j$ is the j'th component of the mass flux vector. In this case the subscript i in (1) is not needed and can be deleted.

[8] We now assume that a one-dimensional layer, having time-independent structure and orientation, moves past an observing spacecraft with constant speed, u_n, along the normal vector, **n**. In a frame of reference moving with the layer, the situation is then time independent so that, using the new variables $x' = x_j n_j - u_n t$ and $t' = t$ (a Galilean transformation), where $\partial/\partial t' = 0$, equation (1) can be transformed to

$$-u_n \frac{d}{dx'}\eta_i + \frac{d}{dx'}\left(n_j q_{ij}\right) = 0. \tag{2}$$

In the definition of x', x_j is the j'th component of the position vector and $t = t'$ denotes time. It is seen that x' is a coordinate in the moving system, along the normal vector **n**. Equation (2) can then be integrated to give

$$-\eta_i u_n + n_j q_{ij} = C_i, \ \ (i = 1, 2, 3, \text{unless suppressed}), \tag{3}$$

where C_i is a vector constant of integration (unless i is suppressed, in which case C is a scalar constant). In ideal circumstances, equation (3) would be exactly satisfied for all M pairs, $\{\eta_i; q_{ij}\}$, calculated from the measurements, using one and the same set of values for u_n, n_j, and C_i. In reality, this ideal situation is unlikely to arise. Therefore, the next step is to define the residue, R, by the quadratic expression

$$R = \frac{1}{M}\sum_{m=1}^{m=M} \left| -\eta_i^{(m)} u_n + n_j q_{ij}^{(m)} - C_i \right|^2. \tag{4}$$

[9] In equation (4), the superscript (m) refers to individual measurements (at a set of points within or near the current

layer) used in the calculation; the total number of these measurements is M. The operation $(1/M)\Sigma$ is what we denote by the angular brackets, $\langle..\rangle$. The objective of the calculations to follow is to determine C_i, u_n, and the vector $\mathbf{n}$, subject to the constraint $|\mathbf{n}|^2 = 1$, in such a way that R is a minimum. The normalization constraint is implemented in the usual way by minimizing $(R - \lambda|\mathbf{n}|^2)$, where λ is a Lagrange multiplier. In other words, we seek the solution to the equations

$$\frac{\partial}{\partial C_i}\left(R - \lambda|\mathbf{n}|^2\right) = 0, (i = 1, 2, 3, \text{unless suppressed}), \tag{5}$$

$$\frac{\partial}{\partial u_n}\left(R^* - \lambda|\mathbf{n}|^2\right) = 0, \tag{6}$$

$$\frac{\partial}{\partial n_m}\left(R^{**} - \lambda|\mathbf{n}|^2\right) = 0, (m = 1, 2, 3), \tag{7}$$

where R^* is the expression for R when the optimal value for C_i, obtained from (5), has been substituted into (4) and R^{**} is the expression for R^* when the optimal value for u_n, obtained from (6), has been substituted into it. This stepwise approach to the optimization is taken to simplify the analysis. It gives exactly the same results as when the equations (5), (6), and (7), with $R^{**} = R^* = R$, are solved in parallel.

[10] In the first step, we find the optimal value for C_i, which we denote by C^*_i, to be

$$C_i^* = -u_n\langle\eta_i^{(m)}\rangle + n_j\langle q_{ij}^{(m)}\rangle, \tag{8}$$

and then

$$R^* = \langle|-u_n\delta\eta_i^{(m)} + n_j\delta q_{ij}^{(m)}|^2\rangle. \tag{9}$$

Here the δ notation signifies deviation of an individual measurement from its average, for example,

$$\delta\eta_i^{(m)} = \eta_i^{(m)} - \langle\eta_i^{(m)}\rangle. \tag{10}$$

[11] In what follows we will usually suppress the superscript (m), when the symbol to which it is affixed appears inside angular brackets, for example, $\langle\eta_i^{(m)}\rangle = \langle\eta_i\rangle$.

[12] In the second step of the optimization, equation (6) gives the following optimal value for u_n:

$$u_n^* = U_j^* n_j = \mathbf{U}^* \cdot \mathbf{n}, \tag{11}$$

where the velocity vector $\mathbf{U}^*$ is given by

$$U_j^* = \frac{\langle\delta\eta_i\delta q_{ij}\rangle}{\langle|\delta\eta_i|^2\rangle}. \tag{12}$$

Note that the repeated index i in (12) implies summation over i, separately in the numerator and in the denominator (except for the case of a scalar conservation law, where the index i, and the associated summations, are simply dropped). The corresponding revised residue is

$$R^{**} = \left\langle\left|\left(-\delta\eta_i U_j^* + \delta q_{ij}\right)n_j\right|^2\right\rangle, \tag{13}$$

which can also be written as the quadratic form

$$R^{**} = n_i Q_{ij} n_j. \tag{14}$$

Here Q_{ij} is the symmetric matrix

$$Q_{ij} = \left\langle\left(\delta q_{ki} - U_i^*\delta\eta_k\right)\left(\delta q_{kj} - U_j^*\delta\eta_k\right)\right\rangle. \tag{15a}$$

[13] In this expression, summation over the repeated index k is implied. By substitution of (12) into (15a), one may also write Q_{ij} in the form

$$Q_{ij} = \frac{\langle\delta q_{ki}\delta q_{kj}\rangle - \left(\langle\delta\eta_k\delta q_{ki}\rangle\langle\delta\eta_k\delta q_{kj}\rangle\right)}{\langle|\delta\eta_k|^2\rangle}, \tag{15b}$$

where, as before, each average, in brackets, contains a sum over the repeated index k.

[14] The final step in the optimization is expressed by equation (7). It is equivalent to finding the eigenvalues, which are represented by lambda in (7), and the corresponding eigenvectors $\mathbf{X}$ of Q_{ij}. The eigenvector, $\mathbf{X}_3$, corresponding to the smallest eigenvalue, λ_3, is our predictor for the normal vector, i.e.,

$$\mathbf{n}^* = \mathbf{X}_3, \tag{16}$$

λ_3 being the corresponding minimum value of the residue. The symmetric nature of Q_{ij} guarantees that all eigenvalues are real and that the eigenvectors for distinct (nonequal) eigenvalues are orthogonal. Because R is a nonnegative quantity, the eigenvalues must also be nonnegative. We have found that if only three data points are used ($M = 3$), any conservation law for a scalar quantity, η, leads to a degenerate $\mathbf{Q}$ matrix for which two eigenvalues are identically zero. This result is of use for validation purposes. On the other hand for three data points, conservation of a vector quantity, η_i, usually leads to three nonzero eigenvalues.

[15] The velocity vector $\mathbf{U}^*$ can be calculated directly from (12) and, once the eigenvector $\mathbf{X}_3$ has been found, the predicted velocity of the discontinuity is then found from (11):

$$u_n^* = \mathbf{U}^* \cdot \mathbf{X}_3. \tag{17}$$

[16] In (16) and (17), the asterisk affixed to $\mathbf{n}^*$ and u_n^* signifies that these are predicted, as opposed to true, values. For brevity, these asterisks are dropped in the remainder of the paper (other asterisks, having different meaning, remain). Note that, unlike the deHoffmann-Teller frame determination [*Khrabrov and Sonnerup*, 1998b], the generic

analysis in its present form does not permit determination of acceleration or deceleration effects.

3. Conservation Laws

[17] In this section we present the specific formulas that result from the generic ones for the standard conservation laws.

3.1. Absence of Magnetic Poles (MVAB, MVAB/HT)

[18] Since (to our present knowledge) no magnetic poles exist, we have

$$\nabla \cdot \mathbf{B} = \frac{\partial B_j}{\partial x_j} = 0, \tag{18}$$

which is of the form of the generic conservation law (1), with $\eta_i = \eta = 0$ and $q_{ij} = q_j = B_j$, (i.e., $\mathbf{q} = \mathbf{B}$). We then see from (15a) or (15b) that

$$Q_{ij} = \langle \delta B_i \delta B_j \rangle, \tag{19}$$

which is the standard variance matrix upon which the MVAB method is based. This application does not produce the velocity $\mathbf{U}^*$ but, with the aid of deHoffmann-Teller analysis, one may write

$$\mathbf{U}^* = \mathbf{V}_{HT}. \tag{20}$$

The current layer speed normal to itself is then $u_n = \mathbf{V}_{HT} \cdot \mathbf{n}$.

3.2. Conservation of Charge (MVAJ)

[19] Here the conservation law is

$$\frac{\partial \rho_e}{\partial t} + \nabla \cdot \mathbf{J} = 0, \tag{21}$$

where ρ_e is the electric charge density and $\mathbf{J}$ is the current density vector. Thus we have $\eta = \rho_e$ and $\mathbf{q} = \mathbf{J}$. Although this application can be developed in its general form from these two identifications, the results are presently not of practical use because ρ_e is extremely small in a space plasma and cannot be directly measured. Therefore we restrict attention to the standard MHD approximation in which the vacuum displacement current is neglected and quasineutrality assumed. Then equation (21) reduces to $\nabla \cdot \mathbf{J} = 0$ and Q_{ij} becomes

$$Q_{ij} = \langle \delta J_i \delta J_j \rangle. \tag{22}$$

This means that the normal vector, $\mathbf{n}$, can in principle be obtained by standard minimum-variance analysis of the current density vectors (MVAJ). To our knowledge, MVAJ has not yet been used with data from a single spacecraft, for the simple reason that it has been, and still is, extremely difficult to directly measure the current density. However, plasma instrumentation may soon reach a sufficient state of accuracy so that the drift velocity of the electron fluid relative to the ion fluid can be reliably measured. Recently the curlometer capability of the four Cluster spacecraft has been used successfully for determination of $\mathbf{J}$ in the magnetopause from Ampère's law [*Dunlop et al.*, 2002] and then in performing MVAJ on the resulting current vectors [*Haaland et al.*, 2004a]. For other applications of MVAJ, the reader is referred to the work by *Pu et al.* [2005] and also *Xiao et al.* [2004].

[20] The MVAB calculation yields, not just a normal vector, but also the average field component along that normal. Similarly, MVAJ will yield a normal vector and an average normal component of $\mathbf{J}$. However, the one-dimensional model that forms the basis of the calculation does not permit a finite normal component of $\mathbf{J}$. The actual value of $J_n = \langle \mathbf{J} \rangle \cdot \mathbf{n}$ can therefore provide an indication of the level of internal consistency in the calculation. Also, if J_n is significantly different from zero, use of the constraint $\langle \mathbf{J} \rangle \cdot \mathbf{n} = 0$ may help improve the normal-vector determination. The implementation of this type of constraint is discussed in section 4.

[21] For MVAJ, the velocity of the discontinuity can be obtained by integrating Ampère's law over the time interval the spacecraft spends in the layer. This method has been described by *Haaland et al.* [2004a]. Timing of the current layer as it moves past the four Cluster spacecraft can of course also be used [e.g., *Dunlop et al.*, 2002; *Haaland et al.*, 2004b], but sometimes suffers from ambiguity in the determination of the required time delays.

3.3. Conservation of Magnetic Flux (MFR, MVACE, MVADB)

[22] Flux conservation is expressed by Faraday's law, which for our purposes we write in Cartesian tensor form

$$\frac{\partial B_i}{\partial t} + \frac{\partial}{\partial x_j}\left(\epsilon_{ijk} E_k\right) = 0, \tag{23}$$

where ϵ_{ijk} is the Levi-Civita tensor. From (23) we can make the identification $\eta_i = B_i$ and $q_{ij} = \epsilon_{ijk} E_k$ (summation over k is implied). After suitable reassignments of the indices, equation (15a) or (15b) then gives

$$Q_{ij} = \langle (\epsilon_{mik} \delta E_k - U_i^* \delta B_m)(\epsilon_{mjp} \delta E_p - U_j^* B_m) \rangle, \tag{24}$$

where, from equation (12),

$$U_i^* = \frac{\langle \delta B_s \, \epsilon_{sik} \delta E_k \rangle}{\langle |\delta B_p|^2 \rangle}. \tag{25}$$

In these expressions, summations over m, k, p, and s are implied. After straightforward manipulations, these expressions become exactly those given by *Khrabrov and Sonnerup* [1998a] for the Minimum Faraday Residue (MFR) method, namely,

$$Q_{ij} = \frac{-\langle \delta E_i \delta E_j \rangle + \delta_{ij} \langle |\delta E_k|^2 \rangle - P_i P_j}{\langle |\delta B_k|^2 \rangle}, \tag{26}$$

where δ_{ij} is the Kronecker symbol and the Poynting-like vector $\mathbf{P}$ is defined as

$$\mathbf{P} = \langle \delta \mathbf{E} \times \delta \mathbf{B} \rangle. \tag{27}$$

As in the work of *Khrabrov and Sonnerup* [1998a], we also find

$$U_i^* = \frac{P_i}{\langle|\delta B_k|^2\rangle}. \tag{28}$$

[23] Faraday's law can in principle also be used in an entirely different fashion. In a purely one-dimensional layer, $\nabla \times \mathbf{E}$ has no component in the direction normal to the layer. Therefore it is possible, in principle at least, to obtain $\nabla \times \mathbf{E}$ from Cluster's curlometer capability, applied to the directly measured electric or to the convection electric field, $-\mathbf{v} \times \mathbf{B}$, followed by minimum variance analysis of the resulting $\nabla \times \mathbf{E}$ vectors (MVACE). The minimum variance eigenvector then serves as a predictor of the direction normal to the layer. The constraint $(\nabla \times \mathbf{E}) \cdot \mathbf{n} = 0$, can be enforced if needed (see section 4). This is intrinsically a multispacecraft technique, requiring data from four or more spacecraft. For Cluster, only the electric field components in the spin plane are measured by the four EFW instruments: The component along the spin axis would have to be inferred from the assumption $\mathbf{E} \cdot \mathbf{B} = 0$, as is commonly done. In the curlometer application, using $-\mathbf{v} \times \mathbf{B}$ as a proxy for $\mathbf{E}$ fails for Cluster because reliable velocities are obtained only from CIS/HIA onboard two of the four spacecraft (C1 and C3), and sometimes from the CODIF part of the CIS instrument on C4. It also follows from Faraday's law that for each spacecraft separately, the quantity $\partial\mathbf{B}/\partial t$ can be treated by minimum variance analysis (MVADB), either without or with the constraint $\partial\mathbf{B}/\partial t \cdot \mathbf{n} = 0$. In these two applications of minimum variance analysis, the velocity of the layer has to be obtained separately (e.g., as $\mathbf{V}_{HT} \cdot \mathbf{n}$). For MVACE, this can also be done in a way analogous to that mentioned in section 3.2 for MVAJ [see *Haaland et al.*, 2004a].

3.4. Conservation of Mass (MMR, MVAV)

[24] The conservation law for mass is

$$\frac{\partial \rho}{\partial t} + \nabla \cdot (\rho \mathbf{v}) = 0, \tag{29}$$

where ρ is the mass density. In this case, $\eta = \rho$ and the transport vector is $\mathbf{q} = \rho\mathbf{v}$. With these expressions, equations (15a) and (12) immediately yield the formulas for MMR given by *Sonnerup et al.* [2004], namely,

$$Q_{ij} = \langle(\delta(\rho v_i) - U_i^*\delta\rho)\big(\delta\big(\rho v_j\big) - U_j^*\delta\rho\big)\rangle \tag{30}$$

$$\mathbf{U}^* = \frac{\langle\delta\rho\delta(\rho\mathbf{v})\rangle}{\langle|\delta\rho|^2\rangle}. \tag{31}$$

[25] In applying these results to actual plasma data from an instrument that lacks mass discrimination, one may either assume all ions to be protons or one may assume a fixed-percentage admixture of heavier ions, moving at the same speed as the protons. If sufficiently precise measurements with mass discrimination were available, MMR could in principle be used separately for each of the species present. Ideally, the normal vector, $\mathbf{n}$, and u_n, obtained for each of the species, would then be the same.

[26] In the special case where the density is constant, the expression (31) for $\mathbf{U}^*$ becomes undetermined. In that case equation (29) gives $\nabla \cdot \mathbf{V} = 0$ so that, in analogy with MVAB, the relevant Q_{ij} matrix becomes $Q_{ij} = \langle\delta v_i \delta v_j\rangle$. This method is denoted by MVAV. It yields a normal vector and a plasma velocity component along that normal but, unless some assumption is made about the nature of the layer (e.g., that it is a tangential discontinuity), it does not give information about the speed u_n of the discontinuity. As is the case for MVAB, this speed can be obtained as $u_n = \mathbf{V}_{HT} \cdot \mathbf{n}$.

3.5. Conservation of Linear Momentum (MLMR)

[27] At the magnetopause, the plasma pressure usually is not isotropic and the anisotropy often changes in the transition from one side of the layer to the other. Within the layer itself the pressure may also not be gyrotropic. Here we incorporate all of these effects by use of the divergence of the full pressure tensor. The momentum conservation law can then be written as

$$\frac{\partial \rho v_i}{\partial t} + \frac{\partial}{\partial x_j}\left[\rho v_i v_j - \frac{B_i B_j}{\mu_0} + \frac{\delta_{ij}|B_k|^2}{2\mu_0} + P_{ij}\right] = 0. \tag{32}$$

where P_{ij} is the pressure tensor. We now identify the generic quantities

$$\eta_i = \rho v_i \tag{33}$$

$$q_{ij} = \rho v_i v_j - \frac{B_i B_j}{\mu_0} + \delta_{ij}\frac{|B_k|^2}{2\mu_0} + P_{ij}. \tag{34}$$

For the case of an isotropic pressure tensor, we have $P_{ij} = \delta_{ij}p$, where p is the scalar pressure.

[28] When the expressions for η_i and q_{ij} are substituted into (12) and (15a) or (15b), the required formulas for U_i^* and for Q_{ij} are obtained. These formulas are algebraically lengthy and are not written out here. The method is referred to as minimum linear momentum flux residue (MLMR) analysis.

3.6. Conservation of Total Energy (MTER)

[29] The conservation law for total energy is

$$\frac{\partial}{\partial t}\left[\left(\frac{P_{ii}}{2} + \frac{\rho|\mathbf{v}|^2}{2} + \frac{|\mathbf{B}|^2}{2\mu_0}\right)\right] + \nabla \cdot \left[\mathbf{v}\left(\frac{P_{ii}}{2} + \frac{\rho|\mathbf{v}|^2}{2}\right) + \mathbf{v} \cdot \mathbf{P} + \mathbf{q}^* + \mathbf{S}\right] = 0. \tag{35}$$

Here P_{ii} is the trace of the pressure tensor, $\mathbf{P}$, so that $P_{ii}/2$ represents the internal energy per unit volume. Also, $\mathbf{q}^*$ is the heat flux vector, $q_k^* = Q_{iik}^*/2$, where Q_{ijk}^* is the full heat flux tensor, and $\mathbf{S} = \mathbf{E} \times \mathbf{B}/\mu_0$ is the Poynting vector. From

the above expression, we identify the density of the conserved quantity as

$$\eta = \frac{P_{ii}}{2} + \frac{\rho|\mathbf{v}|^2}{2} + \frac{|\mathbf{B}|^2}{2\mu_0} \tag{36}$$

and the transport vector as

$$\mathbf{q} = \left[\left(\frac{P_{ii}}{2} + \frac{\rho v_k^2}{2}\right)\mathbf{v} + \mathbf{v}\cdot\mathbf{P} + \mathbf{q}^* + \mathbf{S}\right]. \tag{37}$$

As before, substitution of these expressions into (12) and (15a) or (15b) will give the required formulas for $\mathbf{U}^*$ and Q_{ij}. The explicit formulas are not given here. We refer to this analysis as the minimum total energy flux residue (MTER) method.

[30] In evaluating the Poynting vector, one should ideally use directly measured electric fields. If such measurements, of sufficient accuracy, are not available, the convection electric field, $-\mathbf{v} \times \mathbf{B}$, can be used as a proxy for $\mathbf{E}$, although this step means that electric fields associated with Ohmic dissipation, electron pressure gradients and inertia, and the Hall effect are neglected. The Hall field can be included by putting $\mathbf{E} = -\mathbf{v_e} \times \mathbf{B}$, where $\mathbf{v}_e$ is the measured electron velocity, which then has to have sufficient accuracy.

3.7. Conservation of Entropy (MER)

[31] The law for conservation of entropy can be obtained from (35) by neglecting all dissipative terms, i.e., by dropping viscous dissipation terms, heat conduction, and electrical resistivity. We only write down the simplest case where $P_{ij} = \delta_{ij}p$, $\mathbf{q}^* = 0$, and $\mathbf{E} = -\mathbf{v} \times \mathbf{B}$. By subtracting the mechanical energy law (the scalar product of $\mathbf{v}$ with the momentum equation) from (35), one then finds

$$\frac{\partial}{\partial t}\left[\rho \ \ln\left(\frac{p}{\rho^{5/3}}\right)\right] + \nabla\cdot\left[\rho\mathbf{v} \ \ln\left(\frac{p}{\rho^{5/3}}\right)\right] = 0. \tag{38}$$

This equation leads to the identifications

$$\eta = \rho \ln\left(\frac{p}{\rho^{5/3}}\right) \tag{39}$$

$$\mathbf{q} = \rho\mathbf{v} \ln\left(\frac{p}{\rho^{5/3}}\right). \tag{40}$$

The resulting minimum entropy flux residue (MER) calculation is valid only in rather limited circumstances. It is directly applicable to discontinuities across which no plasma flow occurs: in ordinary MHD, these are tangential discontinuities (TDs) and contact discontinuities (CDs). If plasma flow occurs across the discontinuity and entropy is conserved, then, in MHD, a strictly one-dimensional, time-independent layer must be a rotational discontinuity (RD) in which the density and pressure, and therefore entropy, are individually conserved (a situation that is rarely observed). The situation is then the same as for MMR with constant density: the relevant Q_{ij} matrix, from which the normal direction, and then the average plasma flow speed along the normal, can be derived, becomes $\langle \delta v_i \delta v_j \rangle$ (MVAV). The speed of the discontinuity can be determined by requiring the flow in the frame moving with the discontinuity to be Alfvénic. In practice, MER can probably also be successfully applied to narrow expansion fans (across which entropy is also conserved). It can be generalized to the case of a gyrotropic pressure tensor and double-adiabatic behavior by replacing $\ln(p/\rho^{5/3})$ in the entropy by $\ln(p_\perp^{2/3}p_\parallel^{1/3})/\rho^{5/3}$.

4. Constraints

[32] It is sometimes desirable to determine the normal vector, $\mathbf{n}$, from residue minimization, with the constraint that $\mathbf{n}$ be perpendicular to some known unit vector $\mathbf{e}$. For example, for a tangential discontinuity one might wish to require the predicted normal to be perpendicular to $\langle \mathbf{B} \rangle$, the average measured $\mathbf{B}$ field in the event so that $\mathbf{e} = \langle \mathbf{B} \rangle / |\mathbf{B}|$. As has been pointed out by A. V. Khrabrov [see *Sonnerup and Scheible*, 1998], such a constraint can be implemented by replacing the residue matrix Q_{ij} by $(P_{ik}\, Q_{kn}\, P_{nj})$ where the projection matrix, P_{ij}, (not to be confused with the pressure tensor) is

$$P_{ij} = \delta_{ij} - e_i e_j. \tag{41}$$

This matrix projects any vector to which it is applied onto the plane perpendicular to $\mathbf{e}$. Therefore, when P_{ij} is applied to the vector $\mathbf{e}$ itself, the result is $P_{ij}e_j = 0$ and also $e_i P_{ij} = 0$. On the other hand, when P_{ij} is applied to any vector, $\mathbf{x}$, that is already perpendicular to $\mathbf{e}$, it becomes the identity operator, i.e., $P_{ij}x_j = x_i$, and $x_i P_{ij} = x_j$. We denote the eigenvalues of the symmetric matrix $(P_{ik}Q_{kn}P_{nj})$ by λ_1', λ_2', and λ_3' (in order of decreasing magnitude), with corresponding eigenvectors $\mathbf{X}_1'$, $\mathbf{X}_2'$, and $\mathbf{X}_3'$. Because $P_{ij}e_j = 0$, it is clear that $\mathbf{X}_3' = \mathbf{e}$ and that $\lambda_3' = 0$. The eigenvectors $\mathbf{X}_1'$ and $\mathbf{X}_2'$ are both perpendicular to $\mathbf{X}_3'$ and therefore to $\mathbf{e}$ so that P_{ij} is the identity operator when applied to $\mathbf{X}_2'$ or $\mathbf{X}_3'$. It follows that the expression for the residue corresponding to these two directions can be written as

$$X_{1i}' Q_{ij} X_{1j}' = X_{1i}' \left(P_{ik}Q_{kn}P_{nj}\right) X_{1j}' \tag{42}$$

$$X_{2i}' Q_{ij} X_{2j}' = X_{2i}' \left(P_{ik}Q_{kn}P_{nj}\right) X_{2j}'. \tag{43}$$

In other words, the residues associated with these two directions are the same for $(P_{ik}Q_{kn}P_{nj})$ as for Q_{ij}. The projection simply leads to a cut by the plane perpendicular to $\mathbf{e}$ through the ellipsoid representing the quadratic form $x_i Q_{ij} x_j$. Note that the eigenvalues and eigenvectors of the two matrices are not the same. The constrained estimator for the normal direction is the intermediate eigenvector, $\mathbf{X}_2'$, of $(P_{ik}Q_{kn}P_{nj})$. The corresponding eigenvalue, λ_2', represents the constrained minimum residue.

[33] The formalism described above can be used to implement constraints such as the ones shown in Table 2. The first two of these ($\perp_1$ and $\perp_2$) are appropriate for a tangential discontinuity where no magnetic connection or plasma flow across the layer is allowed. The third constraint ($\perp_3$) is appropriate for a rotational discontinuity across

Table 2. Constraints

Symbol	Constraint	Description	Discontinuity Type[a]
$\perp_1$	no net B-field along normal	$\langle \mathbf{B} \rangle \cdot \mathbf{n} = 0$	TD
$\perp_2$	no plasma flow across discontinuity	$[\langle \mathbf{v} \rangle - \mathbf{U}^*] \cdot \mathbf{n} = 0$	TD, CD
$\perp_3$	Alfvénic flow across discontinuity[b]	$[\langle \mathbf{v} \rangle - \mathbf{U}^* - \alpha \langle \mathbf{B}/\sqrt{\mu_0 \rho} \rangle] \cdot \mathbf{n} = 0$	RD
$\perp_4$	normal perpendicular to $\mathbf{X_{1MVAB}}$	$\mathbf{X_{1MVAB}} \cdot \mathbf{n} = 0$	TD, RD, CD, S
$\perp_5$	no net current across discontinuity	$\langle \mathbf{J} \rangle \cdot \mathbf{n} = 0$	TD, RD, CD, S
$\perp_6$	B-field stationary along normal	$\langle \nabla \times \mathbf{E} \rangle \cdot \mathbf{n} = -\langle \partial \mathbf{B}/\partial t \rangle \cdot \mathbf{n} = 0$	TD, RD, CD, S

[a]TD, tangential discontinuity; RD, rotational discontinuity; CD, contact discontinuity; S, shock.
[b]Here α is the slope of the regression line in the Walén plot. In our application, $\mathbf{V}_A = \langle \mathbf{B} \rangle / \sqrt{\mu_0 \langle \rho \rangle}$ was used.

which a Walén-type relation holds. Here we have allowed for a slope, α, of the regression line in the Walén plot that may not be precisely equal to ±1. In the fourth constraint ($\perp_4$), the normal is required to be perpendicular to the MVAB eigenvector, $\mathbf{X}_1$, corresponding to the largest MVAB eigenvalue, which vector is often well determined and is tangential to the layer. This constraint can sometimes be useful as a complement to other methods, when the orientation of $\mathbf{X}_3$ from such a method is not well determined because the smallest and intermediate eigenvalues are not well separated but the ratio of maximum to intermediate eigenvalue is large, as is often the case. The advantage of this constraint is that it does not require an a priori decision concerning the nature of the discontinuity (TD, versus RD). This is also the case for the fifth constraint ($\perp_5$), which is relevant to the MVAJ method, and for the final constraint ($\perp_6$), which is relevant to the $\nabla \times \mathbf{E}$ and $\partial \mathbf{B}/\partial t$ methods (MVACE and MVADB). In all cases, the underlying assumption is that the discontinuities are one-dimensional.

5. Composite Method (COM and COM*)

[34] As pointed out by *Sonnerup et al.* [2004], results from two or more of the various residue methods described above can be combined in a variety of ways to produce a single prediction of the normal direction and the speed of a discontinuity. This is done by adding a set of suitably normalized and weighted residue matrices, Q_{ij}. The normalization and assignment of weights is not unique. In the example given by *Sonnerup et al.* [2004], only the two matrices from MMR and MFR were used. Normalization was achieved by division of each Q_{ij} by λ_3, its smallest eigenvalue, the rationale being that more emphasis should be placed on $\mathbf{Q}$ matrices that have small values of the smallest eigenvalue. Because the normal vectors from MMR and MFR seemed to be of comparable quality, the weight 1/2 was then assigned to each normalized matrix. However, normalization by λ_3 leads to problems when λ_3 approaches zero. In a general approach, it is better to normalize each $\mathbf{Q}$ matrix by its trace, i.e., by the sum of its eigenvalues. However, a matrix that has its three eigenvalues of comparable size should be given small weight as should a matrix that has poor separation between its two smallest eigenvalues, λ_2 and λ_3. These objectives can be achieved by use of a weight factor of the form $w^k = m^k/\Sigma m^k$, where, the superscript k denotes an individual method (of which we assume there are K) and

$$m^k = \frac{(\lambda_1^k - \lambda_3^k)(\lambda_2^k - \lambda_3^k)}{\lambda_3^k \sqrt{(\lambda_1^k \lambda_2^k)}}. \tag{44}$$

This weight function is inversely proportional to the area of the statistical error ellipse, defined by equation 8.23 of *Sonnerup and Scheible* [1998] and discussed in Appendix A. This means that, if an individual method, for example, MVAB, yields an ellipse with a large major axis but a very small minor axis, it will still be given substantial weight. In such a circumstance the composite normal vector will be driven toward being perpendicular to the $\mathbf{X}_1$ eigenvector of the individual method without necessarily being driven toward the $\mathbf{X}_3$ eigenvector, i.e., toward the normal direction predicted by the individual method. The COM method is not equivalent to the averaging of weighted normal vectors from the individual methods.

[35] The composite normalized and weighted matrix for a chosen data interval can now be written as

$$Q_{ij}^{COM} = \sum_{k=1}^{k=K} \frac{w^k Q_{ij}^k}{Tr\left(Q_{ij}^k\right)}, \tag{45}$$

where the summation is carried out over the K matrices, $Q^k{}_{ij}$, in the set. The weighting and normalization in (44) and (45), while reasonable, are not unique, and may not always be optimal. In particular, one might sometimes assign weight zero to methods that produce outlying normal directions or outlying magnetopause speeds (the results are then denoted by COM*), although the definition of an outlier remains subjective. Experience needs to guide the development of an optimal scheme.

[36] We can also obtain a composite velocity as

$$\mathbf{U}^{*COM} = \sum_{k=1}^{k=K} w^k \mathbf{U}^{*k}. \tag{46}$$

The composite normal vector of the discontinuity is then the eigenvector corresponding to the smallest eigenvalue of Q_{ij}^{COM} and the composite speed of the discontinuity is the component of $\mathbf{U}^{*COM}$ along this vector. Again, it might be desirable to exclude from the sum in (46) those $\mathbf{U}^*$ vectors that produce outlying values of the magnetopause speed, $u_n = \mathbf{U}^* \cdot \mathbf{n}$. If desirable, various constraints can be applied to Q_{ij}^{COM} as described in section 4.

6. Applications

6.1. Overview

[37] We now illustrate the various residue methods by applying them to an encounter with the magnetopause by the Cluster spacecraft (C1, C2, C3, and C4) on 5 July 2001, around 0623 UT, when Cluster was observing the dawn-side

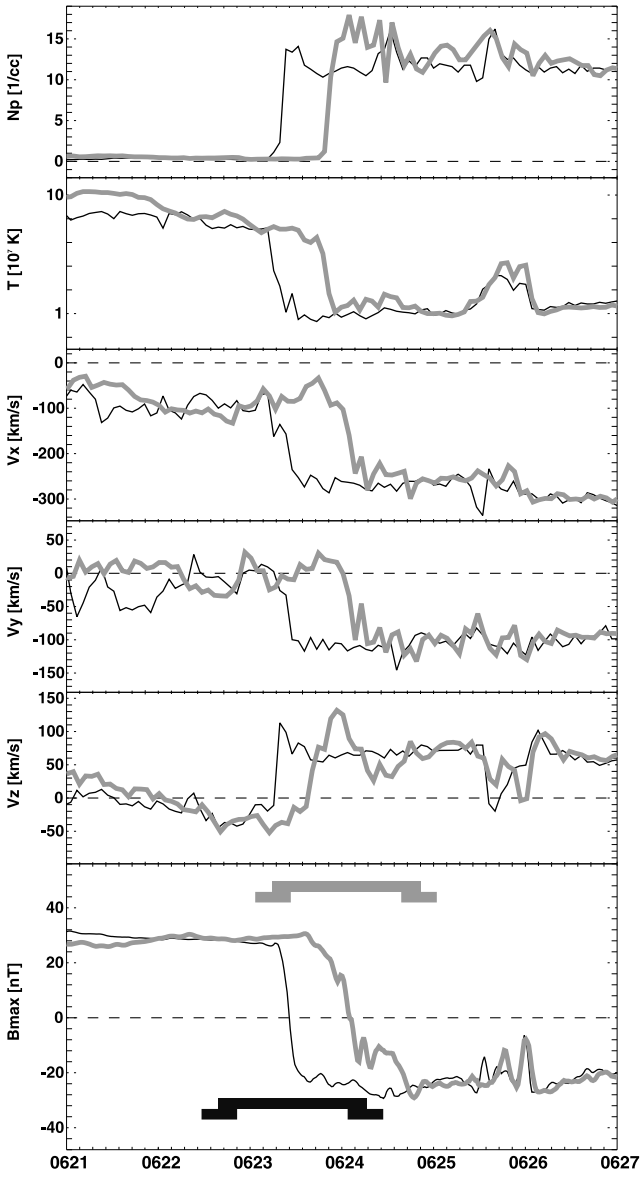

Figure 1. Overview of encounter by Cluster 1 (C1, black curves) and Cluster 3 (C3, gray curves) with the magnetopause on 5 July 2001, around 0624 UT. Approximate spacecraft location was [−6.8, −15.0, 6.2] $R_{E\ GSE}$. Starting at the top, the panels show: time series of measured ion density, temperature and three GSE velocity components from CIS/HIA, and maximum variance magnetic field-component from FGM. The 25-point data intervals used are shown as horizontal bars in the bottom panel, with the seven-nest ranges indicated by shorter bars at each end.

magnetopause as it moved inward past the spacecraft array. During the traversal, the spacecraft C3 had GSE coordinates (X,Y,Z) = (−6.8, −15.0, 6.2) R_E and the spacecraft separations were 2000–3000 km. This event has been studied extensively by *Haaland et al.* [2004b], *Sonnerup et al.* [2004] and *Hasegawa et al.* [2004, 2005]. It is therefore a suitable benchmark case. These earlier studies have indicated substantial time evolution in the time interval between the C1 crossing, where what we interpret as incipient reconnection (Walén slope and correlation: α = +0.57 and cc = 0.975) was seen, and the C3 crossing some 35 s later, where full-blown reconnection (α = +1.03; cc = 0.979) appeared to be at hand. Because of the need for complete plasma measurements in several of the methods, our analysis will be performed only for the traversals by C1 and C3 (C2 and C4 lack CIS/HIA measurements). An overview of the measurements is shown in Figure 1.

[38] For simplicity, scalar pressure and zero heat flux will be used. The spacecraft separations are too large to permit meaningful application of the curlometer to the measured magnetic or electric fields. As mentioned already, variance analysis of $\partial \mathrm{B}/\partial t$ is a feasible single-spacecraft technique. However, to give reasonable results it requires considerable low-pass filtering of the data. In the present event, we then find that the **Q** matrix from MVADB has poor separation between its two smallest eigenvalues, in which case the minimum variance analysis does not give a reliable answer. For this reason we do not report results from MVADB for our test event; illustrative results will be presented elsewhere.

[39] Two main results are obtained from each method: the normal vector orientation and the magnetopause speed. The former are shown in Figure 2 as four polar plots, each with the same bull's eye normal, **n** = (0.584277, −0.811242, 0.022513) GSE, as in the work by *Haaland et al.* [2004b] and *Sonnerup et al.* [2004], where the details of constructing the polar plots are explained. In brief, the bull's eye orientation is the average of the four spacecraft MVAB normal vectors, each composed of the average from seven data nests in the spin resolution data, and each constrained by $\langle \mathbf{B} \rangle \cdot \mathbf{n} = 0$. Note that there is no reason to expect the actual normal direction to coincide exactly with the bull's eye or to be exactly the same for C1 and C3. However, if the component of the magnetic field normal to the magnetopause is small, both the C1 and the C3 normal should be in the vicinity of the bull's eye. The dashed lines in the figure separate regions of positive and negative normal magnetic field components. The lines for C1 and C3 do not coincide exactly and also do not pass exactly through the bull's eye because the C1 line is based on an average field vector $\langle \mathbf{B} \rangle$ from C1 and the C3 line on an average field from C3, whereas the bull's eye normal is constrained by the average field from all four spacecraft.

[40] As in the work of *Sonnerup et al.* [2004], the results for C1 and C3 are presented both for a data set containing M = 25 measurements at spin resolution and for the average over seven nested spin-resolution data sets containing M = 19–31 spin-averaged data points, centered at time 0623:27.5 UT for C1 and at 0624:04.75 UT for C3. In the plots for M = 25, the ellipses centered at the various points represent the statistical uncertainties calculated as derived by *Khrabrov and Sonnerup* [1998c] and described by *Sonnerup and Scheible*'s [1998] equation 8.23. Discussion of these error estimates is in Appendix A. For the seven-nest averages, the ellipses describe the one-sigma spread of the normal vectors derived from the seven individual nest members (see Appendix A). These latter ellipses illustrate the stability of the result under changes in the data interval used. They do not represent an overall uncertainty estimate for the normal vector.

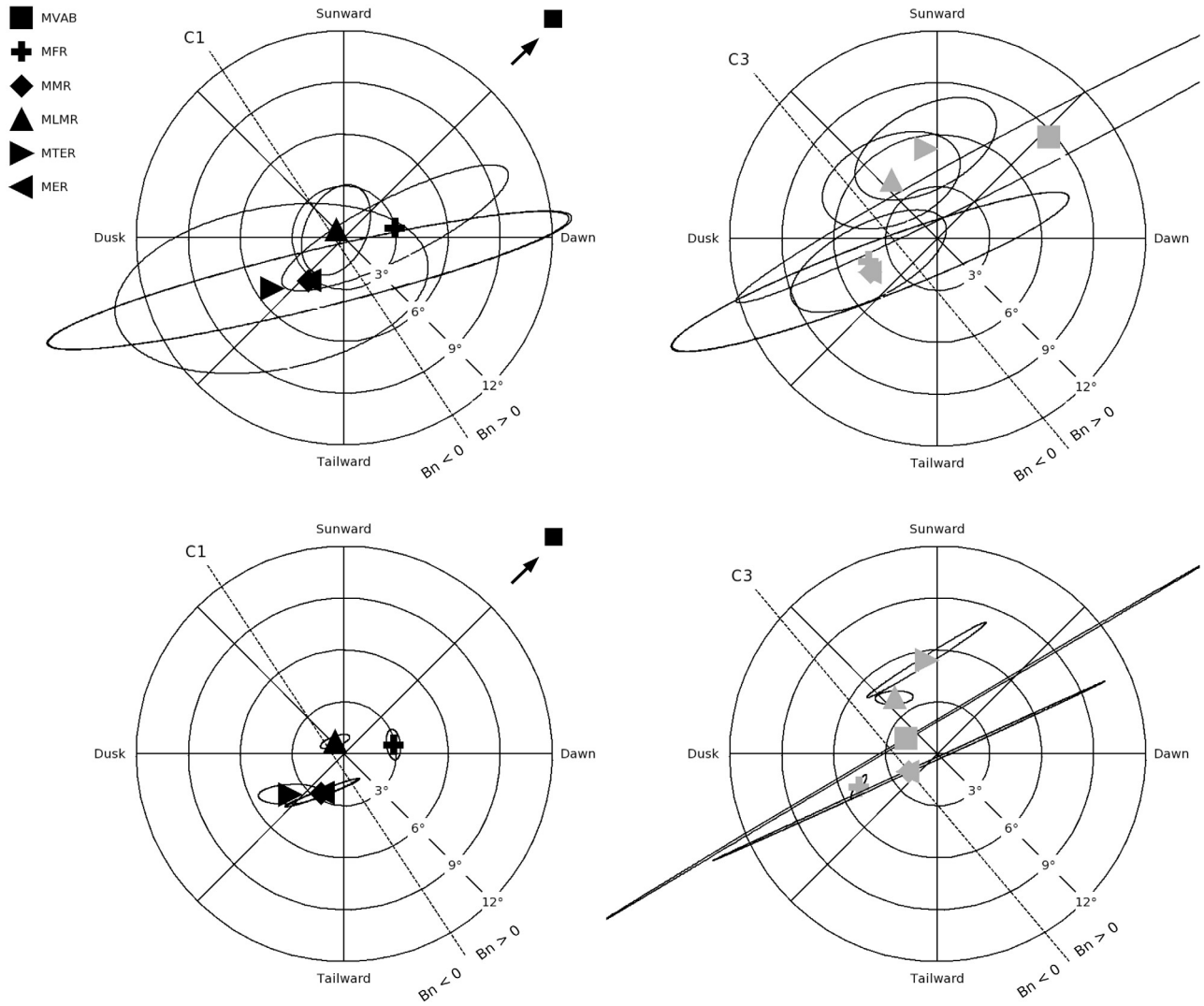

Figure 2. Polar plots representing the orientation of magnetopause normal vectors, calculated from Cluster data taken on 5 July 2001, around 0624 UT, relative to the bull's-eye normal **n** = [0.58428, −0.81124, 0.02251] (GSE components). (top left) Normal vectors derived from Cluster1 (C1, black) 25-point data interval 0622:39.258−0624:15.737 UT, using the various methods. Error ellipses represent statistical uncertainties. Dashed line is locus of normals such that $B_n = 0$. (top right) Same for Cluster 3 (C3, gray) crossing and the 25-point interval 0623:16.663−0625:04.843 UT. (bottom left) C1 results for seven nested segments, with ellipses illustrating the spread of nest member results. (bottom right) Same plot for C3.

[41] Magnetopause normal vectors obtained by use of the constraint $\perp_1$ ($\langle \mathbf{B} \rangle \cdot \mathbf{n} = 0$) are shown in Figure 3 and those from the COM method in Figure 4, in both cases for M = 25. The magnetopause speeds obtained from the different methods are listed in Table 2, along with the normal flow and field components.

6.2. Unconstrained Normal Vectors

[42] The unconstrained normal vectors from C1 and C3 and M = 25 are shown in the top two panels of Figure 2 as the various black (C1) and gray (C3) symbols, respectively. One can see that the unconstrained MVAB normal vectors from both C1 and C3 are outliers. For C1, the normal and its ellipse of uncertainty fall outside the plot (the ellipse major axis is ±12.4°) and the result is only relatively weakly dependent on the length of the data interval used. The reason for this behavior is not clear. As discussed below, for C3 there is a strong dependence of the normal direction on the length of the data interval. With the exception of MVAB, the M = 25 results for both C1 and C3 are clustered within a 6° cone of the bull's eye. The statistical error ellipses are large. For C1 the smallest ellipse comes from MLMR; the corresponding normal vector nearly coincides with the bull's eye normal. Except for MVAB, all the C1 ellipses have a small common region, just tailward of the bull's eye. The true normal should lie somewhere within this region, the size of which should be representative of the domain of statistical uncertainty. We note that the line $\langle \mathbf{B} \rangle \cdot \mathbf{n} = 0$ passes through the common region. From this fact, one concludes that the normal is consistent with $\langle \mathbf{B} \rangle \cdot \mathbf{n} = 0$.

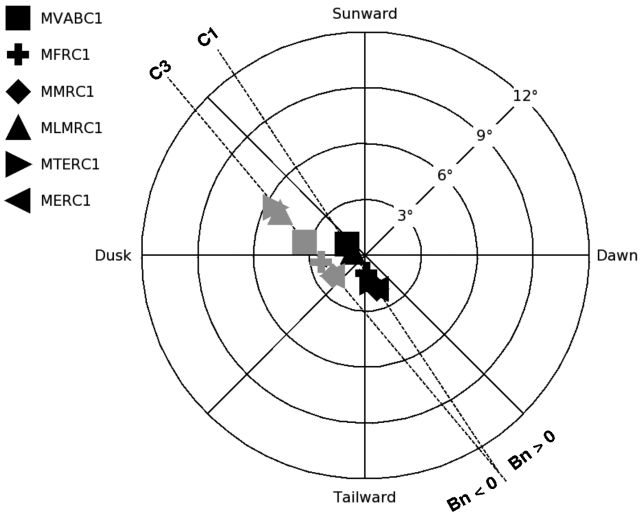

Figure 3. Polar plot for $M = 25$ with the constraint $B_n = 0$ implemented. Both C1 and C3 results are shown, along with the corresponding lines on which $B_n = 0$.

For C3, the situation is more complicated. In this case, none of the normal vectors is closer than 4° to the bull's eye and, even without the MVAB result, there is no region in the plot that falls inside all of the ellipses. There is one narrow domain that describes overlap between MVAB, MLMR, and MTER. All points in this domain have $\langle \mathbf{B} \rangle \cdot \mathbf{n} > 0$. There is a second, very small and narrow domain that describes overlap of the MVAB, MLMR MMR, and MER ellipses and in which $\langle \mathbf{B} \rangle \cdot \mathbf{n}$ is mainly positive. There is also a long, narrow overlap region of the MVAB, MFR, MMR, and MER ellipses. This region extends to substantial negative values of $\langle \mathbf{B} \rangle \cdot \mathbf{n}$ but also has a small part having positive such values. Finally, there is a more substantial overlap region between the ellipses from MFR, MMR, and MER. This region also extends to substantial negative B_n values. On the basis of earlier work on this event [*Haaland et al.*, 2004b; *Hasegawa et al.*, 2004, 2005], we infer that the true normal direction is likely to lie in, or near, the part of this latter region where $\langle \mathbf{B} \rangle \cdot \mathbf{n}$ is negative and that the size of the region is an indication of the domain of uncertainty.

[43] The bottom two panels in Figure 2 show results from averaging over the seven nested data intervals. The purpose of these plots is to illustrate the stability, or lack of stability, of the various normal vectors when modest changes of the data interval (see Figure 1) are made. The orientation of the seven-nest averaged MVAB normal for C1 remains outside the plot but that for C3 is now near the bull's eye. However, the C3 normal vector has an extremely strong dependence on the length of the data interval, as shown by the elongated, narrow ellipse around the average direction (the determination of the ellipse parameters is described in Appendix A). This latter behavior comes from the large uncertainty in the normal vector that accompanies a poor separation of the two smallest eigenvalues in MVAB: The normal vector is narrowly confined to a plane perpendicular to the maximum variance direction but its location in that plane is poorly defined. The event is a good example of a situation where the unconstrained MVAB technique gives poor results. The MMR result for C3 also has a strong dependence on the length of the data interval but, for both C1 and C3, all the other methods give results where this dependence is weak.

[44] Except for the MVAB result, the unconstrained average normal vectors from C1 (black) show remarkable consistency, all lying within a 4° cone around the bull's eye normal, with a bias towards the dusk side and night side (see the bottom left panel in Figure 2). The spread in the C3 (gray) results is somewhat greater: the points all lie within a 6° cone around the bull's eye, with a bias toward the dusk side and day side of the plot (see the bottom right panel in Figure 2).

[45] As mentioned already, the dashed lines in the four plots mark the locus of normal vector points such that $\langle \mathbf{B} \rangle \cdot \mathbf{n} = 0$ for C1 (left plots) or for C3 (right plots). Both for C1 and for C3, negative as well as positive small normal field components are obtained from the various methods (the actual values are given in Table 3 for $M = 25$).

[46] The normal vectors from MMR and MER (and the corresponding ellipses) are very close in all four panels of Figure 2. We have shown that they are also fairly close to the result from MVAV, the reason being that in both MMR and MER the data points in the magnetosheath, where the density and entropy are high and roughly constant, dominate the residue calculation, while the magnetospheric points contribute little. In such a situation, the three methods, MMR, MER, and MVAV should indeed give similar results (see sections 3.4 and 3.7). Because of the presence of the ramps in density and entropy in the magnetopause, both MMR and MER give reasonable and similar predictions for the magnetopause speed, u_n, whereas MVAV on its own does not provide a prediction for u_n.

[47] Returning to the unconstrained normal vectors for C3 and $M = 25$ in the top right plot of Figure 2, we do not know why the MVAB, MLMR, and MTER results for C3 are as

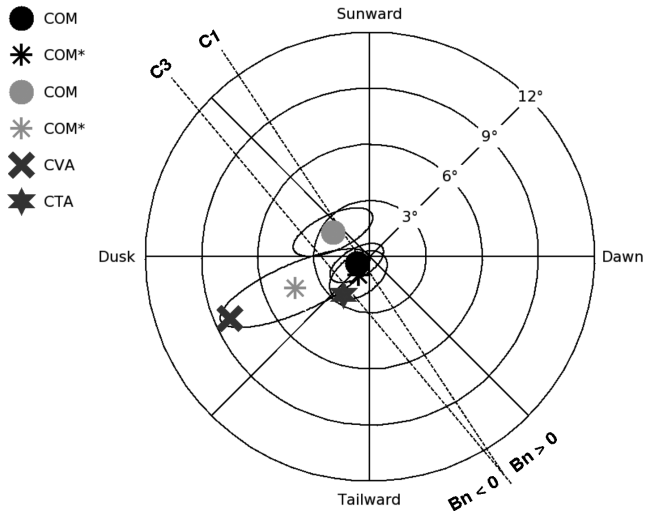

Figure 4. Polar plot for $M = 25$, showing COM and COM* results (C1, black; C3, gray) and the corresponding lines along which $B_n = 0$. For C1, COM* weight zero is assigned to the normal vector from MVAB; for C3, COM* weight zero is assigned to the normal vectors from MVAB, MLMR, and MTER. Error ellipses show statistical uncertainties. Results from two multispacecraft methods (CVA and CTA) are shown for comparison.

Table 3. Magnetopause Normal Velocity, u_n, Plasma Flow Velocity Across the Magnetopause, v_n', and the Normal Magnetic Field Component, B_n[a]

		Cluster 1			Cluster 3		
Method	Symbol in Figures	u_n, km/s	v_n', km/s	B_n, nT	u_n, km/s	v_n', km/s	B_n, nT
MVAB[b]	square	−168.2 ± 4.8	40.4	21.3 ± 2.4	−87.9 ± 61.6	11.8	5.0 ± 9.2
MFR[b]	plus	−69.6 ± 19.4	5.9	1.4 ± 5.9	−47.4 ± 15.8	−1.4	−0.9 ± 5.0
MMR[b]	diamond	−49.3 ± 36.6	−2.2	−1.1 ± 7. 9	−54.6 ± 31.3	7.5	−1.0 ± 7.0
MLMR	triangle, point up	−65.8 ± 22.9	4.2	0.1 ± 5.2	−94.2 ± 23.0	31.5	1.0 ± 4.9
MTER	triangle, point right	−31.1 ± 67.8	−9.0	−1.9 ± 6.2	−149.7 ± 32.9	80.5	2.3 ± 5.0
MER	triangle, point left	−49.5 ± 36.7	−17.3	−1.1 ± 7.9	−54.6 ± 31.3	7.4	−1.0 ± 7.0
COM	circle	−59.1 ± 8.7	0.2	−0.1 ± 5.3	−76.9 ± 10.7	19.2	0.6 ± 4.6
COM*[c]	asterisk	−56.4 ± 9.4	−0.4	−0.2 ± 5.3	−51.2 ± 12.2	3.4	−1.0 ± 5.3
CTA[d]	cross	−54.6	1.5	−0.7	−26.1	−22.9	−0.1
CVA	star	−39.8	−5.6	−3.1	−39.8	−0.6	−2.7

[a]Positive signs indicate outward (away from Earth) directed components. Error estimates are described in Appendix A. Data interval with $M = 25$ is used.
[b]In Table 1 of *Sonnerup et al.* [2004], the sign of $\mathbf{v}'$ was accidentally reversed. Their discussion of this flow component is therefore not valid.
[c]Results from COM when the outlier MVAB is excluded for C1 and the outliers MVAB, MLMR, and MTER are excluded for C3.
[d]Values given by *Haaland et al.* [2004b] have been corrected for a minor computational error.

far off the bull's eye as they are, and on the wrong side of the $\langle \mathbf{B} \rangle \cdot \mathbf{n} = 0$ line, while MFR, MMR, and MER all produce normal vectors and normal field components that are consistent with the reconnection scenario. However, these three methods are not consistently more reliable than the others. For example, in the C1 crossing, the normal vector from MFR, which works well for C3, leads to a non-negligible, positive normal field component (top left plot in Figure 2) when, as mentioned above, the expected result is $\langle \mathbf{B} \rangle \cdot \mathbf{n}$ near zero. On the other hand, the MLMR method, which did not do well for C3, gives an excellent result for the C1 crossing. As our two crossings illustrate, it is not easy to construct methods that consistently produce results that agree with predictions from the Walén test and from Grad-Shafranov (GS) reconstruction.

6.3. Constrained Normal Vectors

[48] Figure 3 shows results for $M = 25$, when the constraint $\perp_1$, namely $\langle \mathbf{B} \rangle \cdot \mathbf{n} = 0$, is implemented. (The results from the seven-nest analysis are not shown but are nearly identical to those for $M = 25$.) As required, all the constrained C1 points, including the MVAB point, now fall on the dashed line, marked C1, that represents satisfaction of this constraint and all fall within a 2° cone around the origin. The small spread of the points along the dashed line indicates that the data are nearly consistent with the constraint $\langle \mathbf{B} \rangle \cdot \mathbf{n} = 0$. In other words, they are consistent with the interpretation of the magnetopause as being very nearly a tangential discontinuity. For C3 all points fall on the dashed line,marked C3, and all fall within the 6° cone around the origin. Both the C1 and C3 lines are oriented duskward/sunward but are displaced from the bull's eye, the displacement of the C3 line being somewhat larger and the spread of the gray points along the line being somewhat larger. Note that the constraint $\perp_1$ is not applicable in the presence of local reconnection and therefore, we believe, should not be used for the C3 crossing. The larger spread of the constrained C3 results could be an indication that the constraint is inappropriate.

[49] Results (not shown) from use of the constraint $\perp_2$ (no plasma flow across the magnetopause) have also been calculated. With this constraint (and $M = 25$), the C1 points from all six individual methods fall in a 3° cone around the origin, a result that is a substantial improvement over the unconstrained results and is again consistent with a tangential discontinuity. The normal field components from the individual methods range from −0.9 nT for MTER to +0.7 nT for MVAB. Within errors, these values are also consistent with a TD. For the C3 points, the constraint is not appropriate because of the ongoing reconnection. And the result is indeed different: the MVAB point and the MFR point both fall inside a 4° cone, while the remaining points are outside, or on, the 8° cone. The normal field component is negative for all methods, except MVAB; it ranges from +0.5 nT for MVAB to −5.2 nT for MMR. As with the C3 results in Figure 3, this behavior suggests that the C3 crossing is not consistent with the assumption of zero flow or zero magnetic flux across the magnetopause.

[50] The constraint $\perp_3$ (Alfvénic flow across the magnetopause) has also been used. For C1, the normal directions are slightly more scattered but all remain within, or on, a 4° cone around the bull's eye. The normal magnetic field and flow components range from −1.4 nT and −6.5 km s^{-1} for MTER to +1.2 nT and +5.8 km s^{-1} for MFR. We conclude that this constraint could also be appropriate for the C1 traversal, even though the results show somewhat larger scatter than do the $\perp_1$ and $\perp_2$ constraints. Therefore this crossing could have been a rotational instead of a tangential discontinuity, albeit with very small negative normal field and flow components. Indeed, for sufficiently small normal field and flow components it becomes essentially impossible to distinguish between the two types of discontinuity. For C3, four of the six methods give normal vectors within, or on, a 4° cone around the bull's-eye normal but the vectors from MTER and MLMR are displaced by 7.3° and 5.4°, respectively, from the bull's eye. The normal field and flow components range from −1.3 nT and −9.8 km s^{-1} for MTER to +2.6 nT and +19.2 km s^{-1} for MLMR. As mentioned already, positive values for $\langle \mathbf{B} \rangle \cdot \mathbf{n}$ and v_n' are inconsistent with the Grad-Shafranov reconstruction results.

6.4. Normal Vectors From Composite Method

[51] We turn now to a discussion of the results from the composite (COM) method. Figure 4 shows the unconstrained normal vector orientations from the $M = 25$ data interval for C1 (black) and C3 (gray), using COM, as described in section 5, with the weights for all methods given by equation (44) (circular dots) and also with the

outliers (MVAB for C1; MVAB, MLMR, and MTER for C3) eliminated completely (COM*: asterix in Figure 4). As described in Appendix A, the ellipse sizes are smaller by a factor $\sqrt{(K-1)}$ than typical ones in the top panels of Figure 2 to account for the fact that $K = 6$ independent methods were combined to form COM and $K = 5$ or $K = 3$ to form COM*. For comparison, we have also shown the normal vectors from two four-spacecraft timing methods, namely the constant velocity approach (CVA) and the constant thickness approach (CTA) [*Haaland et al.*, 2004b]. Of these two results, we believe the one from CTA to be the better one: the CVA assumption of a constant magnetopause speed is poorly satisfied [*Haaland et al.*, 2004b].

[52] As seen in Figure 4, the COM and COM* results for C1 (i.e., with and without MVAB) are very nearly the same. This coincidence of the two normal vector predictions occurs even though the weight for MVAB from equation (44) is not small. Both normal vectors are nearly perpendicular to the $\mathbf{X}_1$ eigenvector from MVAB, the COM vector slightly more so (89.04°) than the COM* vector (88.43°). This result shows that, as mentioned in section 5, inclusion of the weighted $\mathbf{Q}$ matrix from MVAB moves the normal vector a bit closer to being perpendicular to $\mathbf{X}_1$ from MVAB. Within uncertainties, both the COM and the COM* normal vectors are consistent with the results from Grad-Shafranov (GS) reconstruction and from the Walén-test [*Hasegawa et al.*, 2004, 2005], which, taken together, indicate what we interpret as the occurrence of incipient, but not fully developed, local reconnection activity, with an associated very small negative normal magnetic field and flow component (see Table 2). Comparison of the GS reconstruction from C1 with that from C3, less than a minute later, strongly suggests that reconnection was indeed in a state of becoming established [*Hasegawa et al.*, 2005]. When all methods are included, the C3 normal vector from COM falls somewhat on the wrong side of the dashed C3 line, indicating, incorrectly we think, the presence of a small positive normal field component. When the three outliers (MVAB, MLMR, and MTER) are excluded (COM*), the normal field component becomes negative, as required for consistency with the GS reconstruction results and the Walén test, both of which indicate the presence of active reconnection with an inward normal magnetic field component. Since the GS and Walén evidence for this latter scenario is compelling, we conclude that the COM* result for C3 is better than the COM result. However, even the COM* result has an inconsistency: As seen in Table 2, the predicted normal flow across the magnetopause, while small, is outward rather than inward. This behavior is not consistent with the Walén test, according to which $\langle \mathbf{B} \rangle \cdot \mathbf{n}$ and v'_n must have the same sign.

[53] The COM* normal vectors for both C1 and C3 are reasonably close to the normal vector from the four-spacecraft CTA method but substantially removed from the CVA normal vector. We infer that CVA is not the best multi-spacecraft approach for this event. The combination of CVA and CTA introduced by *Paschmann et al.* [2005], and referred to by them as the Minimum Thickness Variation (MTV) method, would be an acceptable compromise. It places the resulting normal vector half-way between the CVA and CTA vectors in Figure 4, which is close to the COM* vector for C3.

[54] Each of the constraints $\perp_1$, $\perp_2$, and $\perp_3$ has been applied to the COM and COM* calculations. For the C1 crossing, all three results are nearly the same as for the unconstrained calculation. For the C3 crossing, constraints $\perp_1$ and $\perp_2$ are not applicable and $\perp_3$ gives outward directed normal field and flow components for both COM and COM*. Disappointingly, the $\perp_3$ constraint again does not help organize the results from the C3 crossing.

6.5. Normal Motion, Flow, and Field Components

[55] Table 2 contains numerical values of the magnetopause speed, u_n, the plasma flow speed across the magnetopause, v'_n, and the normal magnetic field component, B_n. The unconstrained normal vectors from the two upper panels in Figure 2, i.e., for $M = 25$, were used in constructing the table. The table also shows results from CVA and CTA and from COM and COM*. For COM the weights given by equation (44) are used for each method; for COM* the weights for outliers (MVAB for C1 and MVAB, MLMR and MTER for C3) are forced to zero.

[56] The three columns for C1 in Table 2 show that, except for the outlying values from MVAB, the results are consistent, within error estimates, with a tangential discontinuity. The COM* calculation should provide optimal values: the magnetopause moves inward at an average speed of 56.4 km s^{-1}; the plasma flow, v'_n, across the layer is inward (-0.4 km s^{-1}). It is negligibly small, as is the normal component of the magnetic field (-0.2 nT). For C3, the results from MVAB, MLMR, and MTER are outliers, not so much because of poor normal vector directions but principally because the magnetopause speeds and/or the plasma flow speeds across the magnetopause they generate are unreasonably large (see Table 2). Elimination of these three methods from COM to produce the COM* results causes a significant change in the normal vector (see Figure 4). It also leads to a significant decrease in the inward magnetopause speed, u_n, and to a corresponding decrease in the magnitude of the plasma flow speed across the magnetopause. However, v'_n retains its erroneous sign. The normal magnetic field component is now negative as expected from other evidence. Within error estimates, both v'_n and B_n could be consistent with ongoing reconnection but could also be consistent with a tangential discontinuity ($v'_n = 0$ and $B_n = 0$). The size of the statistical uncertainties given in Table 2 highlights the extreme difficulty of obtaining significant results for the plasma flow across the magnetopause and for the associated normal magnetic field component. On the other hand, the consistency of the results for the C1 crossing with the tangential discontinuity model suggests that the results can sometimes be considerably more accurate than suggested by the error estimates. The difficulties for the C3 crossing may have their roots in a violation of the assumption of one-dimensional magnetopause structure, as is indeed suggested by the GS reconstruction map for this crossing.

[57] Comparison of the u_n, v'_n and B_n values from COM* with corresponding values from the four-spacecraft methods, CTA and CVA, indicates that, for C1, the results from CTA are in excellent agreement whereas, for CVA, the agreement is less good. For C3 the comparison gives mixed

results. For CTA, the magnetopause speed is less than for COM* and there is significant plasma inflow across the magnetopause, as expected during reconnection. However, the normal magnetic field component from CTA is negligibly small. For CVA, the u_n magnitude is larger but is still considerably smaller than from COM*. The plasma flow across the magnetopause is negligible both for COM* and for CVA. The normal field component is negative for both COM* and CVA but has larger magnitude for CVA. One reason for the discrepancy may be that the CTA and CVA results are based on the assumption that the normal vector does not change during the entire interval of the crossing by all four spacecraft. However, the single-spacecraft results reported here suggest that the normal direction did in fact change, albeit not by much, in the interval between the crossing by C1 and that by C3. Since the normal velocity components are very sensitive to the orientation of the normal vector, at least part of the discrepancy may have been caused by a small variation of the orientation.

7. Discussion and Conclusion

[58] We have developed and tested a general approach to obtaining the orientation and speed of a current layer from measurements made by a single spacecraft. One may ask why these results are important in the analysis of data from the four Cluster spacecraft. After all, the Cluster configuration permits determination of both orientation and velocity by use of differences in the time and duration of the individual traversals by the four spacecraft of the current layer [*Dunlop et al.*, 2002; *Haaland et al.*, 2004a] or by direct determination of gradients [*Shen et al.*, 2003; *Shi et al.*, 2005, 2006]. There are at least three reasons why the single-spacecraft methods remain important.

[59] 1. One of the current multispacecraft methods, referred to as the Discontinuity Analyzer, or DA for short [*Dunlop et al.*, 2002], actually makes use of normal vectors determined from single-spacecraft methods (up to now, usually MVAB) applied to data from the four spacecraft, thereby permitting the determination of acceleration as well as variations in the thickness of the layer as it moves past the four spacecraft. Accurate single-spacecraft determinations of the normal vectors at the four spacecraft are important for these purposes.

[60] 2. Because the magnetopause structure sometimes changes significantly in the interval between crossings by the individual Cluster spacecraft during an event, there can be significant difficulties obtaining unambiguous time differences. For this reason, and also because of possible temporal changes in the magnetopause orientation during the event, the results from multispacecraft timing analysis are not necessarily better than those from single-spacecraft techniques. Methods such as CVA, CTA, and DA work best for intermediate spacecraft separation: If the separation is too small compared to the width of the discontinuity, the results become sensitive to errors in the time delays; if the separation is too large, curvature effects or temporal changes in orientation tend to render the results less meaningful.

[61] 3. Multispacecraft methods that are based on the curlometer or gradient capability require small spacecraft separations, so that all four spacecraft are simultaneously within the layer, in order to give accurate results. However, the separation strategy for Cluster is such that some of the separation distances will be large during the remainder of the mission, which will force a return to various single-spacecraft methods. Various validations of these methods, described here [see also *Haaland et al.*, 2004b, 2004a; *Sonnerup et al.*, 2004], using data from the early part of the Cluster mission, therefore take on special importance.

[62] Intercomparison of results from the various single-spacecraft methods discussed here shows generally good agreement (Figure 2) but with a few outliers that are readily identified. After these have been removed, it appears that COM* provides normal directions for C1 and C3 (Figure 4) that are accurate within about $\pm 2^\circ$ and $\pm 4^\circ$, respectively. They are consistent, within uncertainties, with the multi-spacecraft result from CTA (only C3 is consistent with CVA). The results for the magnetopause speed (Table 2) show significant scatter and uncertainties, again with some clearly outlying results. The agreement between the COM* and the CTA results is good for the C1 crossing but much less good for the C3 crossing. Normal components of magnetic field and plasma flow (in the moving frame) are the most difficult quantities to obtain. For the event studied, the COM* normal magnetic-field component is nearly zero for the C1 traversal. It is small and negative for C3. The substantial error estimates notwithstanding, this result is consistent with Grad-Shafranov reconstructions of the event [*Hasegawa et al.*, 2004, 2005]. The plasma flow speed, v_n' across the magnetopause, which we expect to be nearly zero for C1 and small but negative for C3, varies a great deal from method to method. The COM* result has the expected behavior for C1 but not for C3. The three constraints we have tested all work well for the C1 crossing. Neither constraint works well for the C3 crossing.

[63] More experience is needed with the various new methods presented in this paper and how they should be combined to provide an overall optimal prediction for the normal vector, the motion of the discontinuity, and the normal components of field and flow. The results from the event studied here are encouraging, but more so for the C1 than for the C3 crossing. For C3, the results may have been compromised by multidimensional structure of the magnetopause.

[64] It is impressive that the plasma measurements, even assuming scalar pressure, have sufficient quality to produce meaningful results from the momentum and energy conservation laws. The importance of including the full measured pressure tensor and perhaps also the measured heat-flow vector, has yet to be investigated.

Appendix A

[65] The statistical error estimates for the normal vector prediction, $\mathbf{n} = \mathbf{X}_3$, shown as ellipses in Figure 2 (top two panels), are calculated from the formula

$$|\Delta\varphi_{ij}| = \sqrt{\left(\frac{\lambda_3}{(M-1)}\,\frac{(\lambda_i+\lambda_j-\lambda_3)}{(\lambda_i-\lambda_j)^2}\right)}, i \neq j, \qquad \text{(A1)}$$

where $\Delta\varphi_{23}$ and $\Delta\varphi_{13}$ are the ellipse semimajor and semiminor axes, respectively, expressed in radians [*Khrabrov and Sonnerup*, 1998c; *Sonnerup and Scheible*, 1998,

equation 8.23]. Also, λ_1, λ_2, and λ_3 are the eigenvalues, in order of decreasing size, of the **Q** matrix and M is the number of data points used in the analysis. The ellipse major and minor axes are along the eigenvectors $\mathbf{X}_2$ and $\mathbf{X}_1$ of **Q**, respectively, while the normal direction is predicted by $\mathbf{X}_3$. This formula was derived by a linear perturbation scheme. For this reason it is not quantitatively accurate when the angular error estimates, $|\Delta\varphi_{ij}|$ are large. Also, it is an estimate of the purely statistical uncertainty and therefore depends on the number of data points as $1/\sqrt{M-1}$. Unless λ_3 increases as the number of samples increases, the error estimate therefore becomes smaller and smaller as M increases. The estimate does not account for systematic errors caused by organized deviations from a one-dimensional configuration. In interpreting the meaning of the ellipses, all of these items need to be kept in mind. Their shortcomings notwithstanding, the ellipses provide a measure of the statistical part of the uncertainties. They are quantitatively useful for comparative purposes when the number of data points is fixed.

[66] The ellipses shown in Figure 4 are also calculated from (A1), except that their size is reduced by the factor $\sqrt{(K-1)}$, since they are produced by combination of **Q** matrices from K independent methods. The ellipses shown in the bottom two panels of Figure 2 are based on the eigenvalues and eigenvectors of the matrix

$$M_{ij} = \frac{1}{M}\sum_{m=1}^{m=M}\left[n_i^{(m)} n_j^{(m)}\right], \tag{A2}$$

where M now denotes the number of nest members used in the calculation (in our case, $M = 7$) and $\mathbf{n}^{(m)}$ is the normal vector prediction from nest member m. The predictor for the nest average of the M normal vectors is the maximum variance eigenvector, $\mathbf{X}_1$, of the matrix M_{ij}; the square root of the intermediate or minimum eigenvalue and the corresponding eigenvector ($\mathbf{X}_2$ or $\mathbf{X}_3$) give the semimajor or semiminor axis length and orientation.

[67] The uncertainties in u_n and B_n, listed in Table 2 were calculated as

$$|\Delta u_n| = \sqrt{[\Delta\varphi_{13}\mathbf{X}_1\cdot\mathbf{U}^*]^2+[\Delta\varphi_{23}\mathbf{X}_2\cdot\mathbf{U}^*]^2} \tag{A3}$$

$$|\Delta B_n| = \sqrt{[\Delta\varphi_{13}\mathbf{X}_1\cdot\langle\mathbf{B}\rangle]^2+[\Delta\varphi_{23}\mathbf{X}_2\cdot\langle\mathbf{B}\rangle]^2}. \tag{A4}$$

These formulas account only for those statistical uncertainties in the normal component of **U*** and of **B** that are produced by the uncertainty in the direction of the normal vector. For simplicity, uncertainties in the vectors **U*** and **B** themselves are not included. This means that the uncertainties in Table 2 are underestimated. In their discussion of MVAB, *Sonnerup and Scheible* [1998], equation 8.24 did include the effect of the uncertainty in **B** by adding the term $\lambda_3/(M-1)$ under the square root in (A4). This type of term is more complicated for the other methods, in particular for u_n, and usually makes only a minor contribution to the error estimate. For consistency, it has not been included in Table 2, not even for MVAB.

[68] **Acknowledgments.** The research was supported by National Aeronautics and Space Administration under grants NAG5-12005 and NNG 05GG26G to Dartmouth College. The work was initiated during an extended visit by BUÖS to the International Space Science Institute, Bern, Switzerland, in 2001–2002. Research at MPE was supported by Deutsches Zentrum für Luft-und Raumfahrt (DLR) under grant 50 OC 01. Parts of the data analysis were done with the QSAS science analysis system provided by the United Kingdom Cluster Science Centre (Imperial College London and Queen Mary, University of London) supported by The Particle Physics and Astronomy Research Council (PPARC).

[69] Zuyin Pu thanks Benoit Lavraud for the assistance in evaluating this paper.

References

Aggson, T., P. J. Gambardella, and N. C. Maynard (1983), Electric field measurements at the magnetopause: 1. Observation of large convective velocities at rotational discontinuities, *J. Geophys. Res.*, *88*, 10,000.

Dunlop, M. W., A. Balogh, and K. H. Glassmeier (2002), Four-point Cluster application of magnetic field analysis tools: The discontinuity analyzer, *J. Geophys. Res.*, *107*(A11), 1385, doi:10.1029/2001JA005089.

Dunlop, M. W., et al. (2006), The curlometer and other multi-point analysis, in *Proceedings of the Cluster and Double Star Symposium - 5th Anniversary of Cluster in Space* [CD-ROM], *ESA SP-598*, Eur. Space Agency, Nordwiijk, Netherlands.

Haaland, S., B. U. Ö. Sonnerup, E. Georgescu, B. Klecker, G. Paschmann, and A. Vaivads (2004a), Orientation and motion of a discontinuity from Cluster curlometer capability: Minimum variance of current density, *Geophys. Res. Lett.*, *31*, L10804, doi:10.1029/2004GL020001.

Haaland, S., et al. (2004b), Four-spacecraft determination of magnetopause orientation, motion and thickness: Comparison with results from single-spacecraft methods, *Ann. Geophys.*, *22*, 1347.

Haaland, S., B. Sonnerup, G. Paschmann, E. Georgescu, A. Balogh, B. Klecker, H. Réme, and A. Vaivads (2006), Discontinuity analysis with Cluster, in *Proceedings of the Cluster and Double Star Symposium: 5th Anniversary of Cluster in Space* [CD-ROM], *ESA SP-598*, Eur. Space Agency, Nordwiijk, Netherlands.

Hasegawa, H., et al. (2004), Reconstruction of two-dimensional magnetopause structures from Cluster observations: Verification of method, *Ann. Geophys.*, *22*, 1251.

Hasegawa, H., B. U. Ö. Sonnerup, B. Klecker, G. Paschmann, M. W. Dunlop, A. Balogh, and H. Rème (2005), Optimal reconstruction of magnetopause structures from Cluster data, *Ann. Geophys.*, *23*, 973.

Kawano, H., and T. Higuchi (1996), A generalization of the minimum variance method, *Ann. Geophys.*, *14*, 1019.

Khrabrov, A. V., and B. U. Ö. Sonnerup (1998a), Orientation and motion of current layers: Minimization of the Faraday residue, *Geophys. Res. Lett.*, *25*, 2373.

Khrabrov, A. V., and B. U. Ö. Sonnerup (1998b), deHoffmann-Teller analysis, in *Analysis Methods for Multi-Spacecraft Data*, edited by G. Paschmann and P. W. Daly, p. 221, ESA Publ. Div., Paris.

Khrabrov, A. V., and B. U. Ö. Sonnerup (1998c), Error estimates for minimum variance analysis, *J. Geophys. Res.*, *103*, 6641.

Lepping, R. P., and P. D. Argentiero (1971), Single spacecraft method of estimating shock normals, *J. Geophys. Res.*, *76*, 4349.

Paschmann, G., S. Haaland, B. U. Ö. Sonnerup, H. Hasegawa, E. Georgescu, B. Klecker, T. D. Phan, H. Rème, and A. Vaivads (2005), Characteristics of the near-tail dawn magnetopause and boundary layer, *Ann. Geophys.*, 1481.

Pu, Z. Y., et al. (2005), Multiple flux rope events at the high-latitude magnetopause: Cluster/Rapid observation on 26 January, 2001, *Surv. Geophys.*, *26*(1-3), doi:10.1007/s10712-005-1878-0.

Shen, C., X. Li, M. Dunlop, Z. X. Liu, A. Balogh, D. N. Baker, M. Hapgood, and X. Wang (2003), Analyses on the geometrical structure of magnetic field in the current sheet based on Cluster measurements, *J. Geophys. Res.*, *108*(A5), 1168, doi:10.1029/2002JA009612.

Shi, Q. Q., C. Shen, Z. Y. Pu, M. W. Dunlop, Q.-G. Zong, H. Zhang, C. J. Xiao, Z. X. Liu, and A. Balogh (2005), Dimensional analysis of observed structures using multipoint magnetic field measurements: Application to Cluster, *Geophys. Res. Lett.*, *32*, L12105, doi:10.1029/2005GL022454.

Shi, Q. Q., C. Shen, M. W. Dunlop, Z. Y. Pu, Q.-G. Zong, Z. X. Liu, and E. Lucek (2006), Motion of observed structures calculated from multipoint magnetic field measurements: Application to Cluster, *Geophys. Res. Lett.*, *33*, L08109, doi:10.1029/2005GL025073.

Sonnerup, B. U. Ö., and L. Cahill (1967), Magnetopause structure and altitude from Explorer-12 observations, *J. Geophys. Res.*, *72*, 171.

Sonnerup, B. U. Ö., and B. G. Ledley (1979), OGO-5 magnetopause structure and classical reconnection, *J. Geophys. Res.*, *84*, 399.

Sonnerup, B. U. Ö., and M. Scheible (1998), Minimum and maximum variance analysis, in *Analysis Methods for Multi-Spacecraft Data*,

edited by G. Paschmann and P. W. Daly, p. 1850, ESA Publ. Div., Paris.

Sonnerup, B. U. Ö., I. Papamastorakis, G. Paschmann, and H. Lühr (1987), Magnetopause properties from AMPTE/IRM observations of the convection electric field: Method development, *J. Geophys. Res.*, *92*, 12,137.

Sonnerup, B. U. Ö., S. Haaland, G. Paschmann, B. Lavraud, and M. Dunlop (2004), Orientation and motion of a discontinuity from single-spacecraft measurements of plasma velocity and density: Minimum mass flux residue, *J. Geophys. Res.*, *109*, A03221, doi:10.1029/2003JA010230.

Terasawa, T., et al. (1996), On the determination of a moving MHD structure: Minimization of the residue of integrated Faraday's equation, *J. Geomagn. Geolectr.*, *48*, 603.

Vinas, A. F., and J. D. Scudder (1986), Fast and optimal solution to the Rankine-Hugoniot problem, *J. Geophys. Res.*, *91*, 39.

Xiao, C. J., Z. Y. Pu, Z. W. Ma, S. Y. Fu, Z. Y. Huang, and Q. G. Zong (2004), inferring flux rope orientation with the minimum variance analysis technique, *J. Geophys. Res.*, *109*, A11218, doi:10.1029/2004JA010594.

A. Balogh, Space and Atmospheric Physics Group, Imperial College, Prince Consort Road, London SW7 2BW, UK. (a.balogh@ic.ac.uk)

M. W. Dunlop, Space Sciences Division, Rutherford Appleton Laboratory, Chilton, Didcot, OXON QX11 0QX, UK. (m.w.dunlop@rl.ac.uk)

S. Haaland and G. Paschmann, Max-Planck-Institut für Extraterrestrische Physik, D-85748 Garching, Germany. (stein.haaland@mpe.mpg.de; goetz.paschmann@mpe.mpg.de)

H. Rème, Centre d'Étude Spatiale des Rayonnements, 9 Avenue du Colonel Roche, F-31028 Toulouse, France. (henri.reme@cesr.fr)

B. U. Ö. Sonnerup, Thayer School of Engineering, Dartmouth College, 800 Cummings Hall, Hanover, NH 03755-8000, USA. (sonnerup@dartmouth.edu)